scientific reports

Check for updates

OPEN

Investigation and prediction of fatigue performance of SLM 316 L stainless steel based on small build orientation variations and heat treatment effects

Andrei Yankin, Asma Perveen & Didier Talamona✉

Additive manufacturing (3D printing) has facilitated the creation of complex structures, including lattices with diverse build angles. Since lattices often face quasi-static and cyclic loads, understanding material properties across a wide range of printing angles, post-processing conditions, and loading scenarios is crucial. This study explores the effects of building orientations beyond conventional 0, 45, and 90 degrees on the mechanical properties of 316 L steel, produced by laser powder bed fusion. Quasi-static and cyclic tensile tests were performed to evaluate mechanical behavior in as-built and heat-treated conditions, followed by predictive model development. The ultimate strength showed a modest variation of 7% in the as-built condition, while the heat-treated state exhibited a greater variation of 13%. Fatigue tests indicated minor differences between conditions in the low-cycle region but larger gaps in the high-cycle region, where heat-treated samples generally showed superior performance. Inclination angle had a greater effect on fatigue life in the as-built state, with horizontal part orientations outperforming vertical ones. The predictive model demonstrated robust reliability, with nearly 90% of data within an accepted scatter factor of less than three. Requiring minimal experimental data (two fatigue curves per condition), the model is valuable for forecasting fatigue behavior in complex lattice structures.

Keywords Build orientation, Fatigue of materials, Selective laser melting, 316L stainless steel, Annealing Heat Treatment, Outcome prediction model

Additive Manufacturing (AM) is an industrial process that creates objects layer by layer using three-dimensional Computer-Aided Design (CAD) models. AM utilizes various types of feedstock materials, such as filaments, liquid resins, or powdered substances, to build products layer by layer, achieving the desired shape[1].

Selective Laser Melting (SLM) is a powder bed fusion technique where lasers selectively fuse powdered materials in a sealed chamber. According to ASTM standards, this process is also known as laser sintering (LS)[2]. Common materials used include Ti-6Al-4 V[3,4], 316 L[5,6], AlSi10Mg[7,8], and Inconel 718[9]. Meanwhile, 316 L stainless steel is widely utilized across sectors like chemical, petrochemical, nuclear, and food industries due to its excellent corrosion resistance, mechanical strength, and ease of welding and forming[10].

During operations, AM 316 L structures experience various load conditions, necessitating their ability to withstand these stresses, with properties thoroughly evaluated and verified. Review papers, such as[11], have discussed the microstructural and mechanical properties of steels across a range of applications. In addition to static or quasi-static loads, 316 L is frequently used in structures subjected to cyclic loads. Consequently, understanding its fatigue behavior and failure mechanisms becomes essential in these contexts.

The fatigue properties of SLM materials can be influenced by several factors, including part position (both the location on the build platform and the build orientation), printing parameters (such as laser power, scanning speed, and layer thickness), and post-processing techniques (including heat treatment, surface finishing, and hot isostatic pressing).

Department of Mechanical & Aerospace Engineering, School of Engineering and Digital Sciences, Nazarbayev University, Astana, Kazakhstan. ✉email: didier.talamona@nu.edu.kz

The effects of surface finishing on fatigue behavior have been examined in various studies. Common finishing methods include machining[12–15], polishing[16,17], shot peening[18,19], and other techniques[20,21]. These studies generally agree that such finishing processes can enhance fatigue performance.

In the literature on heat treatments (HT) for AM 316 L, the most commonly reported methods are stress relief (SR), annealing (ANN), and hot isostatic pressing (HIP). SR is performed at relatively low temperatures that do not alter the microstructure, though there is considerable variation in both the maximum temperatures and durations, ranging from 450 to 650 °C for 3–6 h[13,15,18,21]. In comparison, ANN is carried out at higher temperatures, typically around 1000 °C, with treatment durations ranging from minutes to several hours, often followed by quenching[17,22,23]. HIP, meanwhile, applies an additional pressure of approximately 100–150 MPa for 2–4 h[22,24–27].

Overall, SR typically has little effect on fatigue behavior, though some studies recommend it to achieve optimal fatigue properties and dimensional accuracy in printed parts[17]. As for ANN, the results are mixed — some studies suggest it improves fatigue strength, while others report a reduction in fatigue resistance. This is further supported by a review paper[10], which concludes that neither ANN nor HIP provides clear advantages for the as-built (AB) state.

In AM, the primary axis of a part can be aligned in various directions relative to the build plate, introducing the concept of build or part orientation, also known as the build or inclination angle. This orientation determines the need for support structures, which influences factors such as build time, material usage, surface finish, residual stresses, and mechanical properties. Thus, as noted in a review[28], build orientation plays a critically important role in the design and evaluation phases of AM.

A noticeable amount of the available literature[26,29–33] is devoted to investigating the influence of build angle on the fatigue properties of AM 316 L stainless steel. The findings demonstrate that fatigue strength is sensitive to build orientation. In particular, vertically oriented specimens tend to exhibit lower fatigue resistance compared to those built horizontally.

Notably, the referenced studies primarily focus on the effects of build angles at 0°, 45°, and 90°, without exploring smaller angle increments. To the best of our knowledge, no research has specifically examined the impact of build orientations outside of these angles for 316 L steel. However, when modeling and simulating complex structures like lattices, where struts can adopt a wide range of angles, it becomes essential to investigate the material properties at these broader ranges of printing angles, as demonstrated in studies such as[34–36].

Given that lattices often undergo complex quasi-static and cyclic loads and considering the lack of research on small directional increments for 316 L stainless steel, this study aims to fill that gap. It investigates the mechanical properties under various process and post-process conditions, including both AB and HT states. Furthermore, the research seeks to develop predictive models for the fatigue behavior of the material.

Methods

The research methodology consists of the following key steps:

• **3D Printing and Post-Processing**: Fabrication of 316 L stainless steel samples via SLM, followed by post-processing heat treatment to prepare them for experimental analysis.

- **Microstructural Analysis**: Examination of the microstructure of the prepared samples to assess the effects of the heat treatment processes.
- **Mechanical Testing**: Performing quasi-static and cyclic tensile tests under varying manufacturing conditions to evaluate the mechanical performance of the material.
- **Data Analysis**: Creating diagrams, extracting mechanical properties, and analyzing fracture surfaces to gain insights into the material's behavior and failure mechanisms.
- **Fatigue Life Modeling**: Developing a predictive model to adequately estimate the material's fatigue life based on the experimental findings and analysis.

In this study, commercially available stainless steel 316 L powder was utilized, with particle size distribution (PSD) parameters measured at $D_{10} = 28.8 \pm 0.2$ µm, $D_{50} = 40.3 \pm 0.3$ µm, $D_{90} = 56.2 \pm 0.3$ µm, and a span (S) of 0.681 ± 0.012. The D_{10}, D_{50}, and D_{90} values represent the particle sizes below which 10%, 50%, and 90% of the particles fall, respectively. The span is determined by the formula $(D_{90} - D_{10}) / D_{50}$[37]. Further detailed analyses of the powder characteristics used in this research can be found in[38].

A Renishaw AM400 SLM system was used to produce 316 L samples for mechanical testing. The sample designs for both quasi-static tensile and cyclic experiments are shown in Fig. 1, in accordance with the ASTM E8M and ASTM E466 standards. The tensile sample used for quasi-static testing had a minimum diameter of 6 mm and a gauge length of 36 mm. For push-pull fatigue testing, an 'hourglass' geometry was employed, featuring a reduced gauge section with a smooth, continuous curvature between the grip sections, a minimum diameter of 4 mm, and an overall length of 64 mm.

To fabricate the samples, the Renishaw system was operated using pre-optimized settings specifically designed for 316L stainless steel. Specifically, the 'SS316L_CHESSBOARD' method was applied, featuring a layer thickness of 50 µm, laser power of 200 W, scan speed of 750 mm/s, hatch spacing of 100 µm, and the CHESSBOARD scan strategy. These settings correspond to the CORE printing parameters. The printing process was carried out in an argon atmosphere. Since powder bed preheating can reduce residual stresses and promote a more uniform microstructure[39,40], the build platform was maintained at 170 °C during printing.

The samples were printed at different build orientations, including 0, 45, 55, 65, 75, 85, and 90 degrees relative to build platform, with 90 degrees being perpendicular and 0 degrees being parallel to the platform. Support structures were incorporated during the process. For the horizontally oriented samples, supports extended along

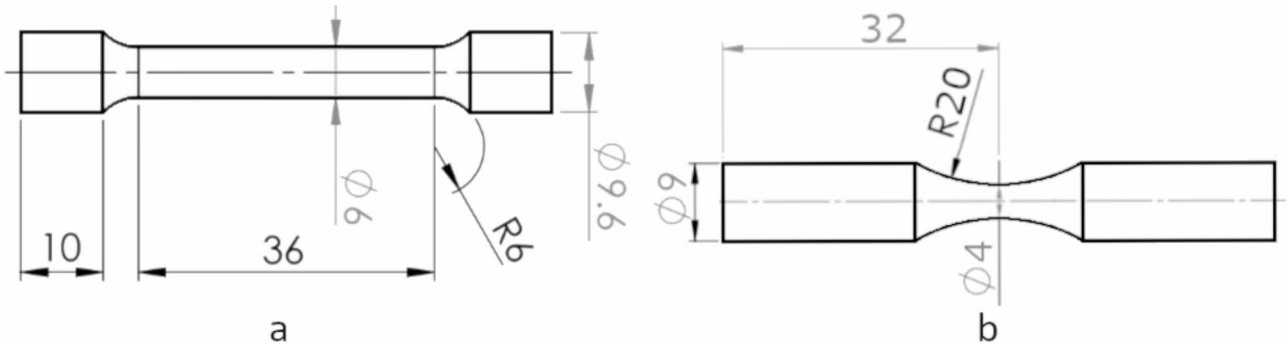

Fig. 1. Illustration of the tensile test sample (**a**) and the fatigue test sample (**b**), with dimensions provided in millimeters.

Experimental set	Building orientation (deg)	Post-processing
As-built (AB)	0, 45, 55, 65, 75, 85, 90	No post-processing
Heat treated (HT)	0, 45, 55, 65, 75, 85, 90	1000 °C for 30 min

Table 1. Design of experiments.

the full length of the sample. For all other angles, the support structures were placed at the circular base and the grip shoulder.

Following the manufacturing process, a portion of the samples underwent post-processing through ANN treatment, while the remaining samples were retained in their AB condition (see Table 1). The thermal treatment was carried out in a muffle furnace, where the samples were heated to 1000 °C and held at that temperature for 30 min. Once the heat treatment was complete, the samples were removed from the furnace and allowed to cool in air at ambient temperature. Next, the samples that received heat treatment in the oven were labeled as HT, while the untreated ones were designated as AB. Importantly, no additional surface treatments, such as machining or polishing, were performed, leaving all samples with their original as-printed surfaces.

Tensile tests were performed using a 'Liangong' universal testing machine, where each sample was subjected to a controlled testing rate of 3 mm/min until failure. Fatigue testing was carried out using the 'HST-P50' fatigue testing system at the stress ratio $R = -1$, with frequencies ranging from 1 to 20 Hz depending on the applied stress amplitude. At lower stress levels, the frequency was set at 20 Hz, while it decreased for higher stress levels.

Fatigue curves are commonly expressed using the well-known Basquin model (see papers such as[41–43]). The equation is typically formulated using the parameters a and b, as shown below:

$$\sigma_a = a \bullet (N)^b \tag{1}$$

where σ_a represents the stress amplitude, while N denotes the fatigue life. Although the Basquin equation is one of the most widely used models, it is not the only one. Several other models can also be employed to describe fatigue behavior (see papers[44,45]).

The Basquin method is a linear model in terms of log-log coordinates. As demonstrated below, an alternative to the Eq. (1) approach can also be expressed using linear-log coordinates:

$$\sigma_a = a \bullet (\log N) + b \tag{2}$$

The Stromeyer model introduces an additional term (σ_∞) to account for the fatigue limit. While this limit may not always occur[46], it remains useful in many engineering applications. The Stromeyer equations are expressed as follows:

$$\sigma_a = a \bullet (N)^b + \sigma_\infty \tag{3}$$

Another widely used approach is the Weibull model, which is outlined below:

$$\sigma_a = (\sigma_u - \sigma_\infty) \bullet \exp\left[-a \bullet (\log N)^b\right] + \sigma_\infty \tag{4}$$

where σ_u is the ultimate strength.

Henry and Dayton proposed:

$$\sigma_a = \frac{a}{N} + b \tag{5}$$

Sendeckyj proposed:

$$\sigma_a = \frac{\sigma_u}{(1 - a + aN)^b} \tag{6}$$

The Hwang and Han approach can be expressed as follows:

$$\sigma_a = \sigma_u \left(1 - \frac{N^b}{a}\right) \tag{7}$$

The power law model is represented by Eq. 8:

$$\log(\sigma_a) = a - b \bullet (\log N)^c \tag{8}$$

The logistic S-N curve model is expressed as follows:

$$\sigma_a = \frac{1 - c}{1 - a + a \bullet \exp[-b \bullet (\log N)]} + c \tag{9}$$

The Kohout-Věchet curve may be represented as:

$$\sigma_a = a \bullet \left[\frac{(N + B) \bullet C}{N + C}\right]^b \tag{10}$$

Microstructural and fracture surface analyses following mechanical testing were performed using a scanning electron microscope (SEM). Before microstructural examination, the specimens were prepared through an etching process using an aqua regia solution to reveal the underlying microstructure. After etching, the samples were thoroughly rinsed with ethanol to remove any residual etchant and prevent contamination.

Results and discussion

Mechanical testing

As noted earlier, all samples were tested in their AB or HT states without undergoing additional surface treatments such as machining or polishing. Consequently, the samples retained their original as-printed surfaces. Surface roughness and subsurface defects, like lack of fusion, act as stress concentrators, initiating fatigue cracks. These cracks propagate progressively under cyclic loading, eventually propagating to a critical size, which ultimately resulted in failure.

The surface roughness R_z varies with the build orientation, measuring 96.5 ± 52.8 µm, 66.5 ± 26.8 µm, 54.1 ± 17.8 µm, 51.5 ± 18.7 µm, 48.7 ± 14.4 µm, 54.2 ± 18.2 µm and 53.4 ± 20.0 µm for build angles of 0°, 45°, 55°, 65°, 75°, 85°, and 90°, respectively. Overall, surface roughness tends to decrease with increasing build orientation from 0° to 65°, stabilizing thereafter. The high roughness at 0° and its large standard deviation are attributed to the presence of support structures extending along the sample's working length on one side. Notably, HT samples exhibited slightly lower surface roughness compared to AB samples. For instance, R_z values for HT samples were 6%, 6%, and 5% lower for build orientations of 0°, 45°, and 90°, respectively - a reduction that is not particularly significant.

The variations in surface roughness, the approximately twofold differences across build orientations, could influence fatigue performance due to higher roughness leading to higher stress concentrations. However, studies such as[47] report no significant influence of surface roughness of similar intensity on fatigue behavior when comparing machined and AB parts. This suggests that the roughness observed in our study may have a limited impact on fatigue performance.

To further evaluate the role of stress concentrators, such as surface roughness, on fatigue resistance, various approaches can be applied[48]. One such approach, the Theory of Critical Distances (TCD), offers guidelines on the maximum defect size that does not decrease fatigue resistance. For instance, defects can be considered negligible if defect sizes (e.g., depth or length) are significantly smaller than the material's critical distance[49].

The critical distance, a material parameter, depends on factors such as the cycle asymmetry, the number of cycles to failure, and microstructural features[50–52]. Therefore, it might be assumed that this parameter may vary under different conditions, such as varying printing parameters or HTs. Consequently, for a deeper understanding of the behavior of materials with rough surfaces, defects, and notches, it is advisable to determine the critical distance experimentally for each specific study rather than relying on values from external research.

The relative density (RD) of SLM-printed 316 L stainless steel was analyzed in this study. Results indicated that RD remains consistent across different building directions, showing minimal variation. For the AB state, RD ranged from 99.6 to 99.9% (a difference of only 0.3%), while for the HT condition, RD ranged from 99.5 to 99.9% (a difference of 0.4%). On average, the RD in the AB state was slightly lower at 99.7% compared to 99.8% in the HT condition. However, this difference is statistically insignificant.

Energy Dispersive Spectroscopy (EDS) analysis provided insights into the chemical composition of 316 L stainless steel across different build angles and under both AB and HT conditions. The results confirmed that the elemental composition of 316 L remains consistent across build orientations and processing conditions. Specifically, the Si content ranged from 0.3 to 0.5%, Cr from 17.3 to 17.7%, Mn from 0.6 to 0.8%, Fe from 67.3 to 68.4%, Ni from 10.1 to 10.6%, and Mo from 2.2 to 2.8%. Neither the AB nor HT conditions resulted in

statistically significant changes in the chemical composition. Additionally, variations in oxygen content were minimal, the average value was around 0.5%.

The chemical composition results provided above are associated with the core material of the printed parts. However, an oxidation layer may form on the specimen surface, particularly under HT conditions. To investigate this, EDS mapping was conducted (see Fig. 2). Figure 2 clearly illustrates the presence of oxidation on the surface of the HT sample. In contrast, AB samples did not exhibit surface oxidation differing from the core composition. To determine the depth of the oxidation layer, the intensity of chemical elements was measured along a line extending from the sample surface into the core. The results indicate an average oxidation thickness of 16.3 ± 8.9 µm. In this region, elevated oxygen concentrations were observed, averaging $31.0 \pm 4.5\%$, sharply decreasing to 0.5% beyond the oxidation boundary. There were no significant differences in oxidation observed across the various build orientations.

As highlighted in the literature[53–55], thermal oxidation can have a notable impact on reducing the fatigue resistance of various alloys. According to Lima et al.[55], the formation of a brittle oxide layer fosters brittle fracture mechanisms, thereby shortening the fatigue crack nucleation period. Meanwhile, at low crack growth rates, oxides located on the crack path can act as obstacles, resulting in crack deflection and subsequently increasing the overall crack growth length[56].

Surface post-processing techniques, such as machining and polishing, can be effective at removing oxidation layers. However, applying these methods to complex structures might be challenging. Therefore, this study focuses on AB parts to generate insights that can be extended to modeling such complex geometries.

Figure 3 presents the microstructure analysis of printed 316 L stainless steel (sample cross-section). The loading and build directions are shown in Fig. 3q, while a 3D schematic of the sample with supports is presented in Fig. 3r. The microstructure can be analyzed at varying scale levels, referred to as the mesoscale, which corresponds to lower magnifications (Fig. 3a, c, e, g, i, k, m, and o) and microscale with higher magnifications (Fig. 3b, d, f, h, j, l, n, and p)[57]. At the mesoscale, the microstructure of AB samples reveals a distinct layer-wise morphology. This is attributed to the manufacturing process, where overlapping and layer stacking result in noticeable fusion interfaces within the SLM-formed layers.

The macrostructure of the 0-degree sample cross-section features overlapping semi-circular melt pools (Fig. 3a), influenced by the rotation of the scanning direction with each layer. This rotation causes the scanning direction to vary relative to the section. When parallel or nearly parallel, continuous stripes resembling those in transverse Sect. (90-degree sample in Fig. 3m) form instead of melt pools. As a result, the melt pools deviate from an ideal semi-circular shape, appearing more elongated in one direction. The melt pools of 0-degree samples are 40–90 µm in width and 100–450 µm in length.

The transverse section, parallel to the build plate (90-degree samples), exhibits overlapping hatch lines with distinct laser tracks oriented in varying directions (Fig. 3m). This variation in orientation arises from the rotation of the hatch pattern after each layer. The width of the stripes remains relatively consistent, averaging approximately 100 µm, while their length measures around 200–700 µm.

Intermediate building orientations, such as 45° and 65°, represent a gradual microstructural transition between the 0° and 90° samples (see Fig. 3e, i), with feature sizes remaining intermediate between these orientations.

In addition to analyzing melt pool boundaries, grain sizes were measured as well. For the AB state, grain sizes do not show significant variations across different build angles, averaging 21 µm. The grains exhibited irregular shapes and can grow across layers, the effect was also reported in studies[58,59]. The aspect ratio (AR) of the grains tended to decrease with increasing build orientation. Similar findings were reported in[60]. The AR was highest at 2.8 ± 1.6 for 0°, then decreased to 1.9 ± 0.7, 2.1 ± 0.6, 2.0 ± 1.0, 2.2 ± 0.9, and 1.8 ± 0.6 for 45°, 55°, 65°, 75°, and

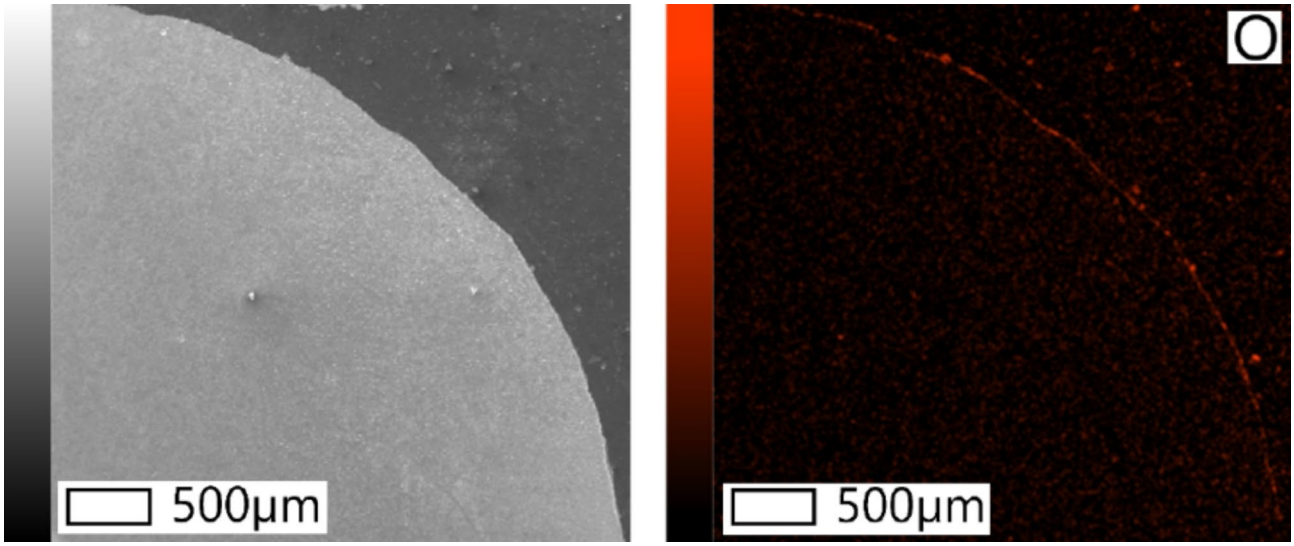

Fig. 2. Cross-section of the 316 L sample showing an oxidized surface layer formed after heat treatment.

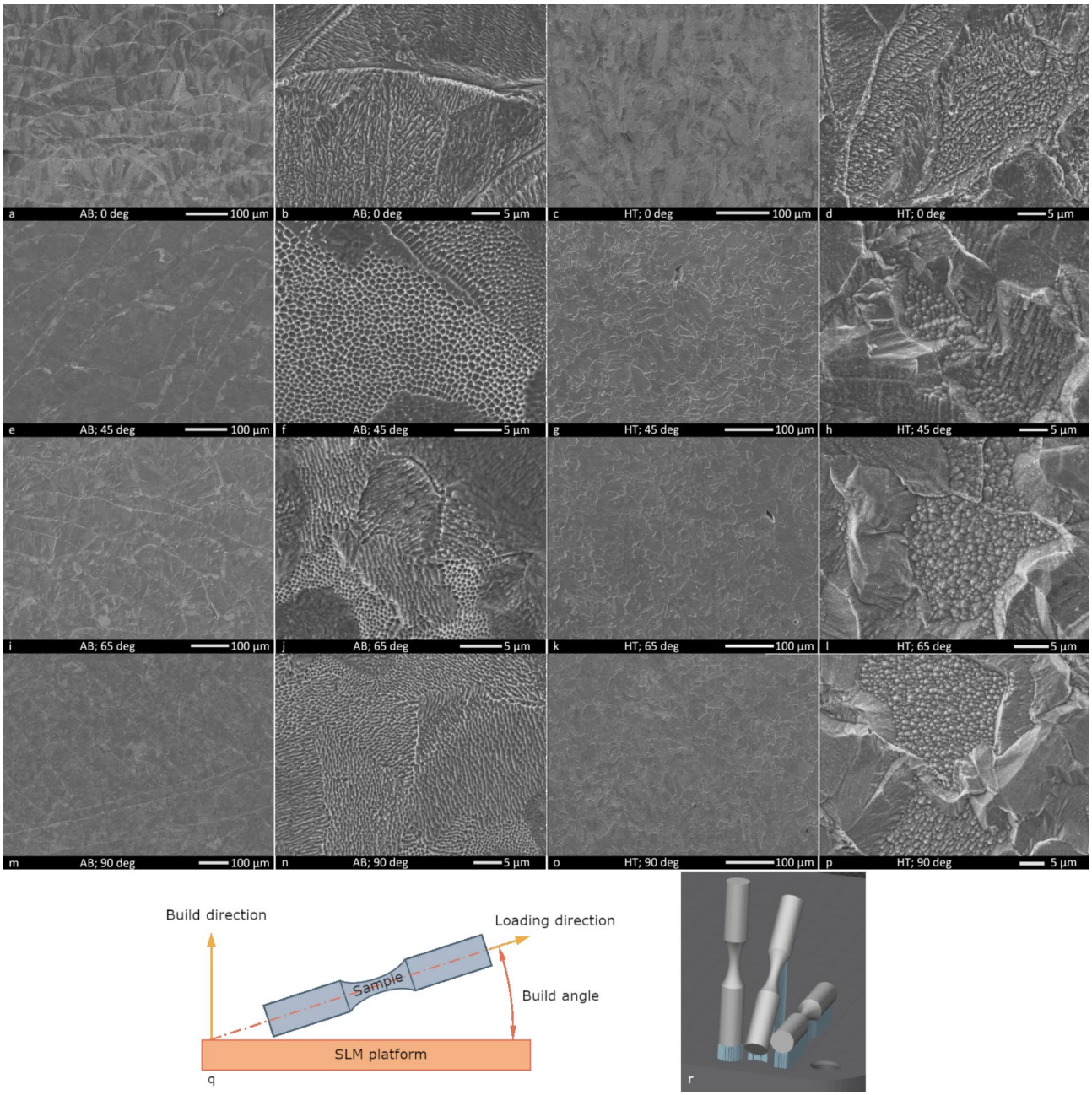

Fig. 3. Microstructure observed in the cross-section of 316 L stainless steel sample produced via SLM in the AB condition (**a**, **b**, **e**, **f**, **i**, **j**, **m**, **n**) and after HT (**c**, **d**, **g**, **h**, **k**, **l**, **o**, **p**) at build angles of 0° (**a**, **b**, **c**, **d**), 45° (**e**, **f**, **g**, **h**), 65° (**i**, **j**, **k**, **l**), and 90° (**m**, **n**, **o**, **p**), displayed at lower magnifications (**a**, **c**, **e**, **g**, **i**, **k**, **m**, **o**) and higher magnifications (**b**, **d**, **f**, **h**, **j**, **l**, **n**, **p**). Schematic representation of the sample, showing the loading and build directions (**q**). A 3D schematic representation of samples with supports oriented at 0°, 45°, and 90°, prepared using QuantAM V5.1 (renishaw.com/en/software-for-laser-powder-bed-fusion-metal-3d-printing-systems–15255) build preparation software (**r**).

90°, respectively. Also, it is important to note that the standard deviations remained relatively high, indicating substantial variability.

At the microscopic level, a distinct sub-grain structure is observed. In the AB condition of 316 L stainless steel, the structure is characterized by small columnar and equiaxed cellular sub-grains[58,61–63]. These sub-grains grow predominantly perpendicular to the fusions. Similar findings have been reported in the literature[64]. Additionally, various clusters of columnar grains can exhibit varying orientations, emphasizing the complexity of the microstructure. The shell regions within the subdomains exhibit a brighter appearance compared to the core areas, suggesting an enrichment of heavy elements like Mo and Cr in the shell. This phenomenon has been documented in prior studies[65,66]. The localized accumulation of these elements is likely a result of the rapid solidification rate.

The size of the cells is governed by the solidification rate, which is influenced by the time-temperature history during the printing process[57]. The cellular sub-grains typically exhibit a low AR, averaging around 1.3, indicating an almost equiaxed shape. The cell sizes were measured as 349 ± 66 nm, 373 ± 165 nm, 367 ± 120 nm, 429 ± 113 nm, 416 ± 234 nm, and 375 ± 97 nm for build orientations of 0°, 45°, 55°, 65°, 75°, and 90°, respectively. This data suggests that at lower build angles, the cells have a tendency to be slightly smaller. In contrast, columnar sub-grains display significantly higher ARs, ranging from 3 to 23, reflecting their elongated structure. The size of these columnar sub-grains fluctuated moderately between 1.2 and 1.5 µm, with standard deviations of approximately 0.6 µm. The size and AR showed no strong correlation with build orientation.

Generally, the grain and sub-grain sizes can influence the fatigue resistance of 316 L steel, with smaller sizes being more favorable for extended fatigue life and larger sizes associated with shorter fatigue life[67,68]. Kamaya[68]observed that the effect is more pronounced in the high-cycle fatigue regime compared to the low-cycle regime. Additionally, variations in molten pool boundaries can influence fatigue crack propagation, as demonstrated in a study on AlSi10Mg[69].

Platform heating and the additional heat introduced into the solidified layers during the application of new layers can act as an in-situ HT process[70,71]. The temporary increase in temperature can promote atomic diffusion and dislocation movement. Therefore, the temperature input is assumed as a crucial role in shaping the microstructure and determining the properties of AM-built materials[72]. Additionally, the boundary conditions for heat dissipation vary depending on the printing orientation and the presence of supports[73]. The number of supports required differs with building angles, being highest at 0 degrees and lowest at 90 degrees. Collectively, heat dissipation, pre-heating, and in-situ HT can significantly affect the static and cyclic mechanical properties of the material, resulting in variations across different build orientations and conditions.

Following the application of HT, particularly ANN, the melt pool boundaries characteristic of SLM fabrication vanish (Fig. 3c, g, k, o), with grain boundaries becoming more distinct. This effect intensifies as the HT temperature increases. The effect of melt pool boundary disappearance during HT has been documented in other studies[74–78]. Because of the significant structural transformations induced by HT, direct comparisons between the AB and HT states become challenging.

The sub-grain microstructure diminishes significantly after HT but remains partially visible in the SEM micrograph (Fig. 3d). Generally, cellular structures begin to dissolve when heated to temperatures above 400–600 °C and are completely eliminated at 1000–1100 °C[79]. The persistence of this structure after heating at 1000 °C for 30 min might be attributed to the limited dwell time during HT. For comparison, extended HT durations, such as 6 h, have been shown to completely dissolve cellular microstructures[76].

The HT process reduces the concentration of Mo and Cr at the cell boundaries compared to the AB state[66,79,80]. This slow dissolution of Mo and Cr is thought to exert a pinning effect, preserving the cellular structure even at high temperatures. Kong et al.[81]attributed the high thermal stability of the cellular structure to the relatively low stored energy in the 3D-printed material. Also, HT can result in a reduction in dislocation density and residual stresses[82].

The HT process significantly reduced structural anisotropy. Nevertheless, the grain formation was uneven. The measured grain sizes were 21.5 ± 8.4 µm, 20.2 ± 10.4 µm, 20.1 ± 13.3 µm, 18.0 ± 10.5 µm, 23.1 ± 11.1 µm, and 20.6 ± 7.8 µm for build orientations of 0°, 45°, 55°, 65°, 75°, and 90°, respectively. The substantial variations in grain size can be attributed to diverse mechanisms of grain evolution, including the fusion of initial grains and cells, recrystallization, and the growth of recrystallized grains, among others[79]. Overall, there appears to be no correlation between grain size and build orientation.

Thus, AB samples exhibit the anisotropic nature of the material structure in 316 L stainless steel, with variations in building direction from 0° to 90° influenced by the melt pool boundaries, as well as the size and shape of grains and sub-grains. This structural anisotropy can lead to anisotropic fatigue behavior. With the application of HT, the melt pool boundaries disappear, and sub-grains merge and transform into austenitic grains[63], resulting in a more isotropic material. Avanzini[10] also noted that the application of ANN may result in more isotropic crack propagation, which can be advantageous under lower cyclic stress conditions.

In this study, fatigue testing was conducted across a broad range of fatigue life, ranging from one cycle to a million cycles. The lower limit, a fatigue life of one cycle, corresponds to the material's ultimate tensile strength (UTS), which was determined using tensile specimens (Fig. 1a). At this stage, no fatigue damage was considered, as the focus was on measuring the material's maximum load-bearing capacity before failure. Other experiments focused on fatigue behavior, employing dedicated fatigue specimens (Fig. 1b).

The results of the quasi-static tensile tests are presented in Table 2 and illustrate the effect of ANN and build orientation on the ultimate tensile strength (UTS). The data are reported as mean values alongside their corresponding standard deviations, with the coefficients of variation provided in brackets in Table 2. The coefficients of variation[83] were computed using the following equation:

$$CoV = \frac{100 \times SD}{x_m} \tag{11}$$

where SD represents the standard deviation and x_m denotes the mean value.

For the AB condition, UTS values range from 560.0 MPa to 601.3 MPa, showing a modest variation of 7%. In contrast, the HT condition exhibits a more noticeable variation, with UTS values ranging from 543.9 MPa to 627.1 MPa, a difference of about 13%. The dependence of UTS on build angle is more pronounced in the HT condition compared to the AB condition (13% vs. 7% variation, respectively). Additionally, differences between the AB and HT conditions, accounting for variability, were observed in only three cases: at build angles of 0 degrees (6%), 55 degrees (7%), and 85 degrees (9%), all of which still indicate relatively small differences.

Build angle	Ultimate tensile strength, MPa		Yield strength, MPa	
	AB	HT	AB	HT
0 deg.	588.1 ± 11.6 (2.0%)	627.1 ± 4.5 (0.7%)	456.8 ± 32.4 (7.1%)	345.4 ± 13.5 (3.9%)
45 deg.	598.1 ± 3.5 (0.6%)	583.7 ± 25.2 (4.3%)	457.3 ± 34.1 (7.5%)	313.5 ± 30.2 (9.6%)
55 deg.	560 ± 24.4 (4.4%)	603.1 ± 3.3 (0.6%)	461.1 ± 1.0 (0.2%)	333.5 ± 8.0 (2.4%)
65 deg.	599.4 ± 6.5 (1.1%)	593.9 ± 10.1 (1.7%)	457 ± 5.1 (1.1%)	343.2 ± 5.9 (1.7%)
75 deg.	601.3 ± 3.6 (0.6%)	595.9 ± 12.2 (2.0%)	448.1 ± 2.0 (0.4%)	333.8 ± 14.3 (4.3%)
85 deg.	596.4 ± 5.4 (0.9%)	543.9 ± 21.9 (4.0%)	440.5 ± 11.9 (2.7%)	283.9 ± 1.2 (0.4%)
90 deg.	575.3 ± 16.2 (2.8%)	578.6 ± 22.6 (3.9%)	430.5 ± 7.9 (1.8%)	312.6 ± 15.5 (4.9%)

Table 2. Ultimate tensile and yield strength values in MPa.

It is important to emphasize that the temperature gradient and local heat dissipation significantly influence grain growth in the structure of AM products, leading to variations in the microstructure across different build orientations. These microstructural changes directly impact mechanical properties such as UTS and YS, which tend to increase with higher cooling rates[84]. For instance, tensile testing results revealed an increasing trend in UTS up to a 75° build angle, followed by a decline in the AB condition. However, the observed fluctuations are limited to approximately 7% and are unlikely to have a practically significant effect.

Fatigue tests were performed across various stress amplitudes, from approximately 199 MPa to 517 MPa, corresponding to roughly 0.35–0.90 of the material's UTS. At higher stress levels, the testing frequency was set to 1 Hz to accommodate the plastic deformation typically associated with low-cycle fatigue. Conversely, as the stress levels decreased and the fatigue tests transitioned into the high-cycle fatigue region, the frequency was increased to 20 Hz to accelerate testing while minimizing material heating effects.

The results, summarized in Table 3, demonstrate the influence of ANN, build orientation, and stress amplitude on fatigue life. This dataset was then used to develop S-N curves using Eqs. (1–10). For each equation, the mean absolute error (MAE) between the experimental and predicted stress amplitude values was computed. The S-N curves with the lowest MAE, which best represent the fatigue data, are shown in Fig. 4. In Fig. 4, as well as in similar figures (Figs. 5, 6, 7 and 8), curves and experimental data are depicted using unique colors to differentiate between conditions (AB or HT) and building angles. Additionally, experimental data are assigned distinct marker shapes or line styles in grayscale to improve clarity when color alone is insufficient.

According to the results, the values show minimal variation in the lower fatigue life region, but the difference becomes more pronounced in the higher fatigue life region, particularly at stress levels around 199 MPa. Specifically, for almost all build orientations, the fatigue life in the HT condition is longer than that in the AB condition. An exception is observed at a 0 degrees build angle, where the AB sample ran out, while the HT sample failed after approximately 900,000 cycles.

The influence of build orientation on fatigue performance is more significant in the AB condition than in the HT condition, particularly in the high-cycle fatigue region. This difference is likely attributed to the anisotropic macrostructure of 316 L steel in the AB state (refer to Fig. 3). In the AB condition, fatigue performance decreases as the build angle increases, with horizontally oriented samples demonstrating a longer fatigue life compared to vertically oriented ones. Post-printing HT reduces the structural anisotropy and mitigates the differences in fatigue performance across various build angles, as previously noted.

The analysis of fracture surfaces are presented in Fig. 9, on the example of the 0-degree samples, where fatigue cracks were mostly initiated from defects near the surface. As the fatigue test progressed, the crack propagated, with the region involved in this phase displaying relatively smooth surfaces - a result of the repeated interaction and movement of the crack surfaces. Eventually, the crack reached a critical size, leading to rapid propagation and catastrophic failure.

In summary, several factors influence fatigue life, including inherent printing defects (such as lack of fusion, porosity, and high surface roughness), material oxidation, and microstructural features (such as the size and shape of grains, sub-grains, and melt pool boundaries). These factors collectively exert positive and negative effects on fatigue performance, impacting crack initiation and propagation. Furthermore, their behavior can vary under different conditions, such as during initiation versus propagation phases or in low-cycle versus high-cycle fatigue regimes that even more complicate the interpretation. Therefore, more specific and comprehensive investigations are needed.

The models (Eqs. 1–10) were used to determine the best-fit curves. Specifically, the equation with the lowest error from Eqs. 1–10 was selected for each build angle and for both the AB and HT conditions. To estimate the model parameters, the Levenberg-Marquardt method was applied, solving the least squares problem. Figure 5 visually compares the model predictions with the experimental results, offering a clear assessment of each model's predictive accuracy relative to the experimental data. The vertical axis of the graph depicts the predicted values from the best-fit models (Eqs. 1–10), each tailored to specific build angles for both the AB and HT conditions.

AB state				HT state			
No	Stress amplitude (MPa)	Fatigue life (cyc)	Build angle (deg)	No	Stress amplitude (MPa)	Fatigue life (cyc)	Build angle (deg)
1	517	736	0	39	398	5544	0
2	398	12,670	0	40	350	18,000	0
3	350	48,538	0	41	279	131,440	0
4	279	242,467	0	42	239	99,047	0
5	239	121,272	0	43	199	874,944	0
6	199	run out	0	44	517	686	45
7	398	33,146	45	45	462	289	45
8	350	16,681	45	46	398	3563	45
9	279	122,004	45	47	350	19,495	45
10	239	421,386	45	48	279	107,962	45
11	199	514,496	45	49	239	426,685	45
12	517	84	55	50	199	run out	45
13	398	4183	55	51	279	208,688	55
14	350	21,285	55	52	239	178,281	55
15	279	70,836	55	53	239	184,067	55
16	239	139,870	55	54	199	run out	55
17	199	166,013	55	55	398	4030	65
18	517	34	65	56	350	13,541	65
19	398	6415	65	57	279	84,982	65
20	350	6409	65	58	239	run out	65
21	239	104,282	65	59	239	591,323	75
22	199	150,907	65	60	199	540,253	75
23	398	37,155	75	61	350	4574	85
24	350	25,908	75	62	279	40,808	85
25	279	113,600	75	63	239	250,270	85
26	239	136,324	75	64	199	667,556	85
27	199	189,507	75	65	398	1096	90
28	517	92	85	66	350	14,571	90
29	398	3754	85	67	279	195,026	90
30	350	14,310	85	68	239	163,123	90
31	279	93,278	85	69	199	run out	90
32	239	189,691	85				
33	199	286,333	85				
34	398	3541	90				
35	350	27,409	90				
36	279	92,595	90				
37	239	92,030	90				
38	199	126,276	90				

Table 3. Fatigue test results.

The horizontal axis, on the other hand, represents the experimentally measured fatigue life values. Diagrams like the one shown in Fig. 5are commonly used to evaluate prediction accuracy in material fatigue studies (e.g., see papers[85–87]).

In Fig. 5 and similar diagrams below, the solid black line represents perfect agreement between predictions and test results. Points to the left of this line indicate predictions that are overly optimistic, while points to the right indicate more conservative predictions. The dashed lines mark a scatter range of ± 2 factors, and the dash-dotted lines mark a scatter range of ± 3 factors. "± factors" means that the actual results may differ by up to two or three times the predicted value. For instance, if the predicted fatigue life is 1000, the ± 2-factor range would be from 500 to 2000, and the ± 3-factor range would be from 333 to 3000. To make prediction errors easier to interpret, specific markers are used:

- Circles: Errors within the ± 2-factor range.
- 'X' Marks: Errors within the ± 3-factor range.
- Squares: Errors outside the ± 3-factor range.

The analysis shows good agreement between the model's predictions and the experimental data for both the AB and HT conditions. Specifically, 57 out of 69 samples (82.6%) fall within the ± 2-factor error range, leaving

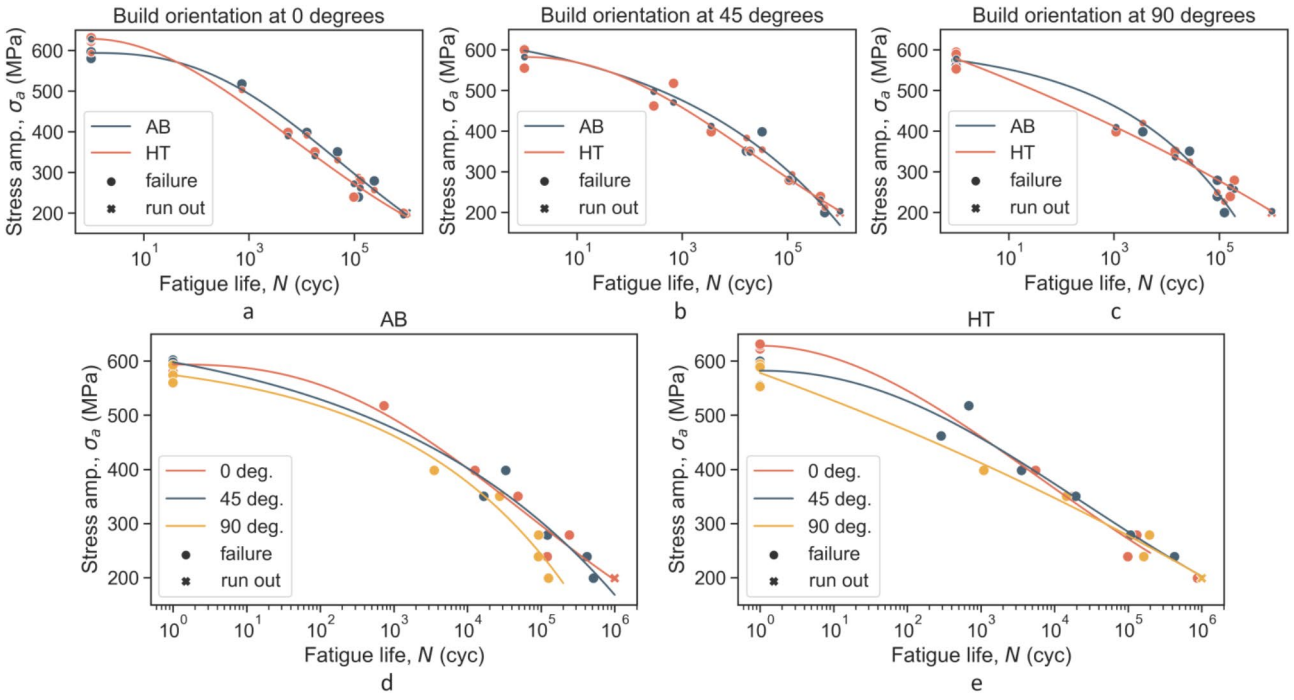

Fig. 4. Fatigue test results for 316 L stainless steel at build angles of (**a**) 0 deg, (**b**) 45 deg, and (**c**) 90 deg, under AB (**d**) and HT conditions (**e**). *Curves and experimental data are represented using unique colors to distinguish different conditions (AB or HT) (**a**, **b**, **c**) and building angles (**d**, **e**). Additionally, experimental data are assigned unique marker shapes: black dots and crosses are used to indicate either failed or run-out samples, corresponding to the respective colors.

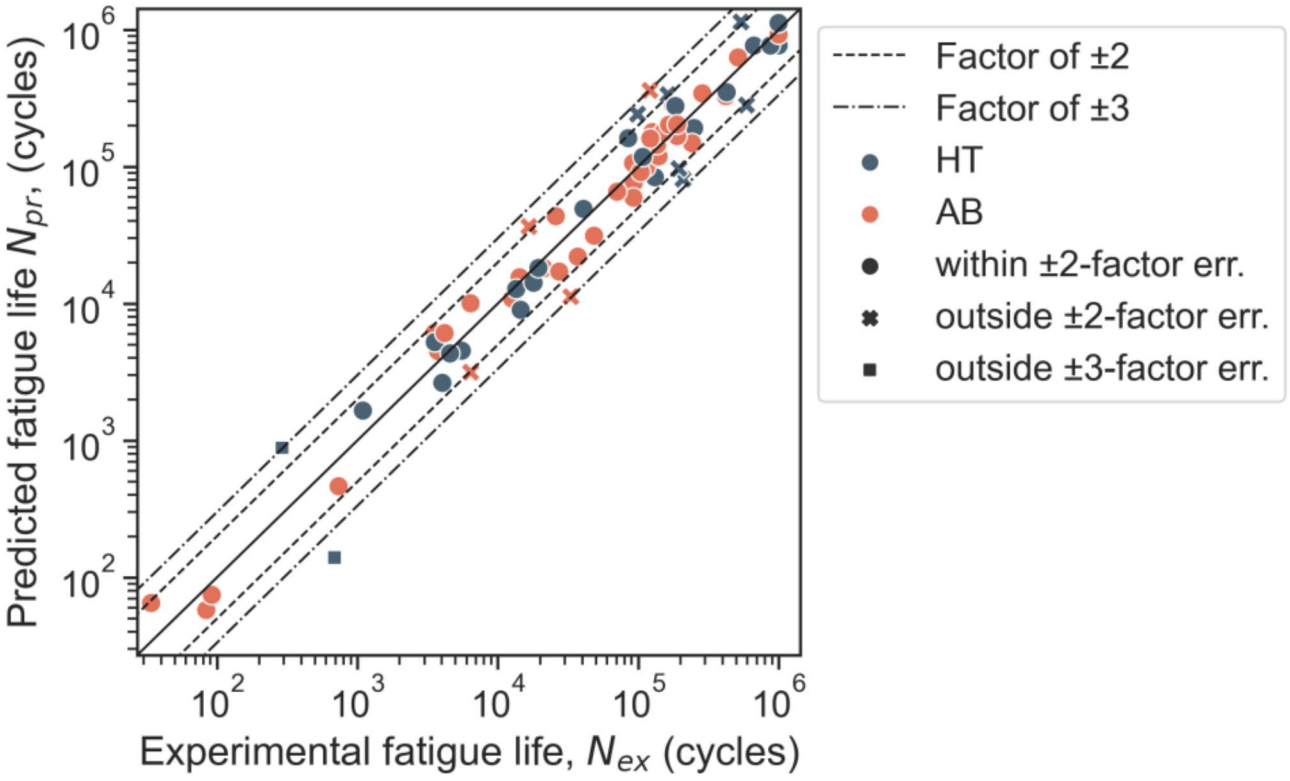

Fig. 5. Comparison of the predictions from best-fit curves (RA model) with experimental results. *The colors of the experimental points indicate AB and HT conditions, while the shapes of the points and the line styles represent error factors.

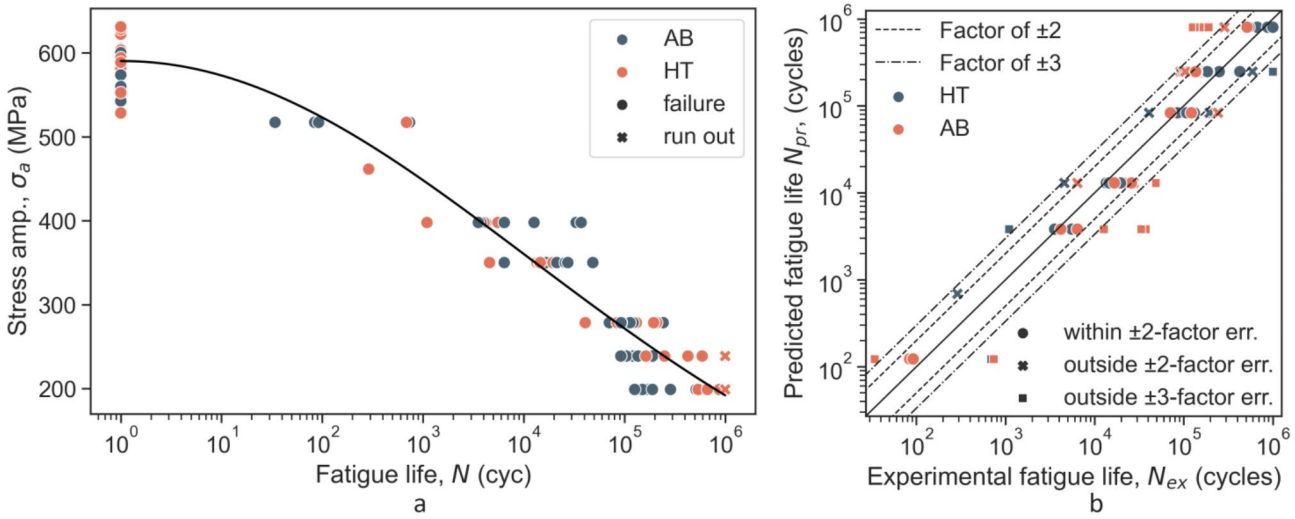

Fig. 6. Predictions of the PLM model across all data (**a**) and comparison of the predictions with experimental results (**b**). *The colors of the experimental points indicate AB and HT conditions, while the shapes of the points represent experimental outcomes (failure or run-out) in (a) and prediction results (error factors) in (**b**).

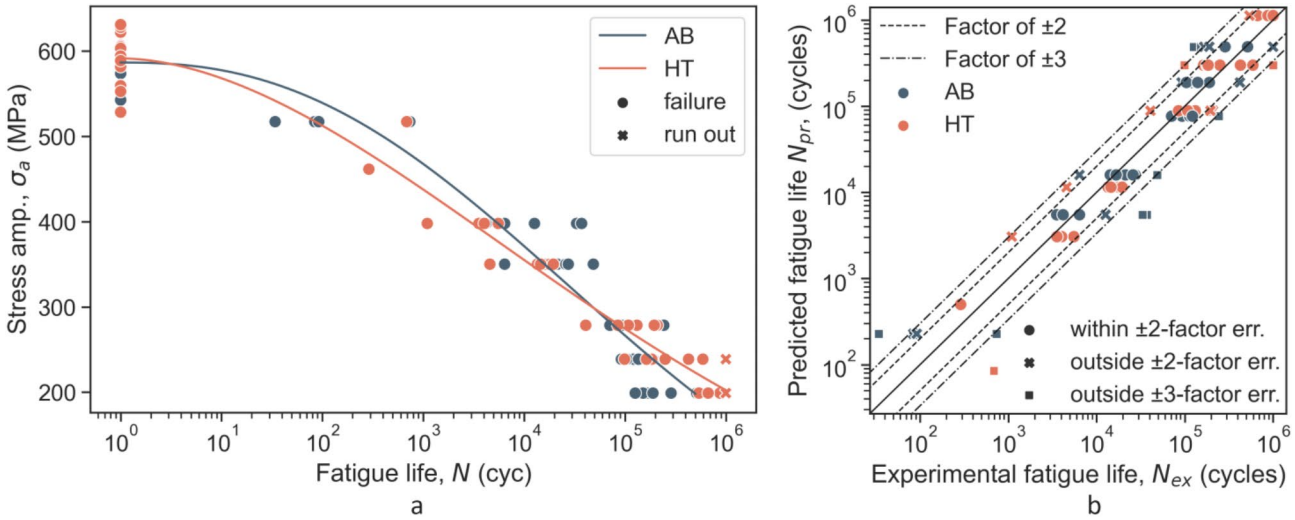

Fig. 7. Predictions of the PM model across all data (**a**) and comparison of the predictions with experimental results (**b**).*The colors of the experimental points and curves indicate AB and HT conditions, while the shapes of the points represent experimental outcomes (failure or run-out) in (**a**) and prediction results (error factors) in (**b**).

17.4% of results outside this range. Only 2 out of 69 samples (2.9%) fall beyond the ± 3-factor error range. The Root Mean Squared Error (RMSE) between the predicted and experimental fatigue life is approximately 0.213 on a logarithmic scale, equivalent to a ± 1.63-factor error. Additionally, the RMSE between the predicted and experimental stress amplitudes is around 16.7 MPa. Moving forward, these accuracy metrics will be referred to as the Reference Approach (RA), which serves as a benchmark for predictive models.

Fatigue life modeling

During the development of the predictive model, the following methodology was applied: initially, a single model curve was used to describe all the data; the model was then incrementally refined, first by accounting for the AB and HT conditions, and subsequently by incorporating build orientation; after each refinement, key metrics were calculated to assess the model's accuracy, including the percentage of results within the ± 2-factor error range, those beyond the ± 3-factor error range, and the RMSEs for both fatigue life and stress amplitude, as described earlier (see Fig. 5 and its description); finally, all the metrics were compared to the reference values mentioned earlier (see Fig. 5 and its description).

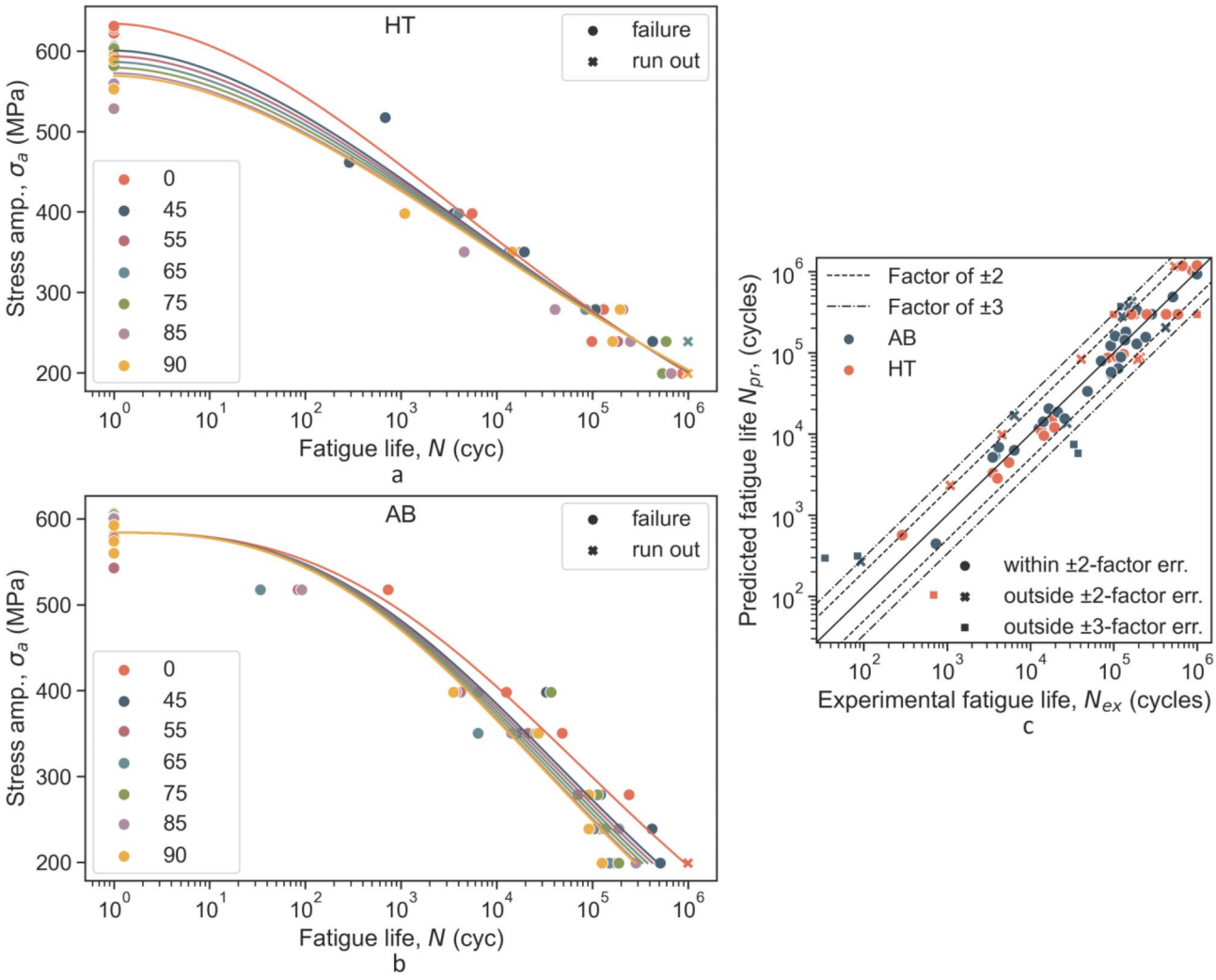

Fig. 8. Predictions of the PBOM model under HT (**a**) and AB (**b**) conditions, with a comparison to experimental results (**c**). *The colors of the experimental points and curves indicate building angles in (**a**, **b**) and AB and HT conditions in (**c**), while the shapes of the points represent experimental outcomes (failure or run-out) in (**a**, **b**) and prediction results (error factors) in (**c**).

Among all the models, the power law model delivered the most accurate results and was thus applied to the entire dataset:

$$\log_{10}(\sigma_a) = 2.77 - 0.0129 \bullet [\log_{10}(N)]^{2.03} \tag{12}$$

Specifically, the model parameters were determined using the least squares method, minimizing the error between the experimental data and the predicted results.

In Fig. 6a, the prediction results are presented for the entire dataset, while Fig. 6b illustrates the comparison between the predictions and experimental outcomes. The data reveals that 42 out of 69 samples fall within the ± 2-factor error range, leaving 39.1% of results beyond this threshold. Additionally, 13 out of 69 samples (18.8%) fall outside the ± 3-factor error range. The RMSE for fatigue life is approximately 0.372 on a logarithmic scale, equivalent to a ± 2.36-factor error, while the RMSE for stress amplitude is around 27.8 MPa. Next, this approach will be referred to as the Power Law Model (PLM).

The second approach is enhanced to account for HT post-processing, referred to as the Post-Processing Model (PM). This introduces a categorical variable that distinguishes between the AB and HT conditions, which must be handled appropriately. A simple method can be used, where two new variables are created: one for the AB state and another for the HT state. In this encoding, the AB variable is set to 0 when HT is applied, and vice versa—the HT variable is 0 when no heat treatment is applied, leaving the parts in the AB condition. A similar approach has been previously applied in other studies[88,89]. The model can be written as follows:

$$\text{For AB: } \log_{10}(\sigma_a) = 2.77 + 0.00673 \bullet [\log_{10}(N)]^{2.44} \tag{13}$$

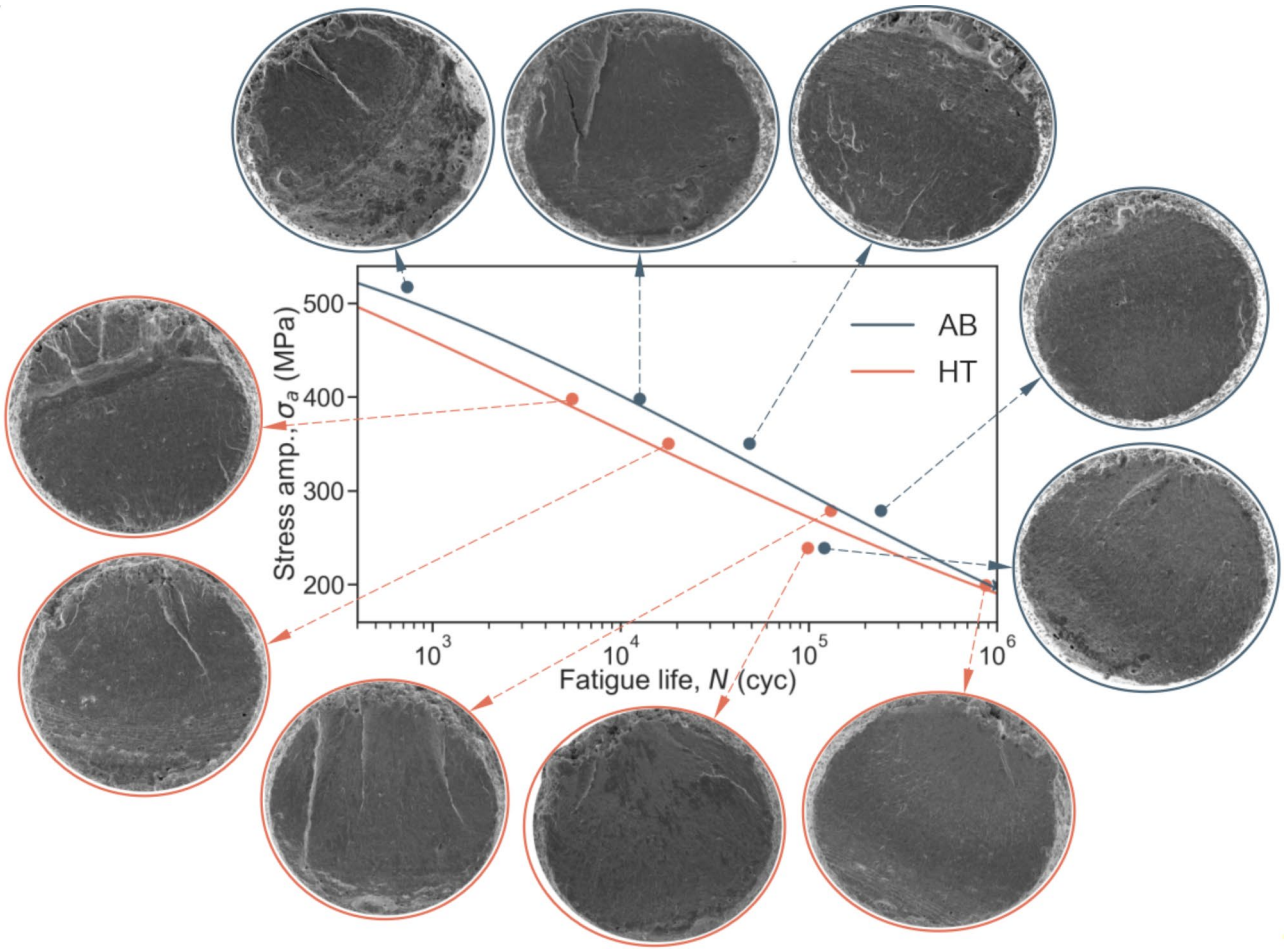

Fig. 9. Fracture surfaces of SLM 316 L stainless steel 0-degree samples from fatigue tests conducted under AB and HT conditions.

$$\text{For HT: } \log_{10}(\sigma_a) = 2.77 + 0.0175 \bullet [\log_{10}(N)]^{2.77}$$

To determine the model constants, the dataset was divided into two parts: one containing experimental results for AB samples and the other for HT samples. Each subset was then used to calculate the model parameters using the least squares method.

In Fig. 7a, the prediction results from the PM are presented for both the AB and HT subsets, while Fig. 7b provides a comparison between the model predictions and experimental results. Upon close examination of the graphs, it becomes clear that HT parts exhibit a longer fatigue life than AB parts in the high-cycle region, where materials are subjected to lower stress over more cycles. Conversely, in the low-cycle region, where the material experiences higher stress over fewer cycles, the AB parts demonstrate superior fatigue performance compared to the HT samples.

Additionally, 43 out of 69 samples lie within the ± 2-factor error range, with 37.7% of results exceeding this threshold. Also, 11 out of 69 samples (15.9%) are outside the ± 3-factor error range. The RMSE for fatigue life is approximately 0.339 on a logarithmic scale, corresponding to a ± 2.18-factor error, while the RMSE for stress amplitude is about 27.0 MPa. Overall, this model offers slightly improved predictions compared to the PLM, reinforcing the observation that the ANN influences fatigue performance.

The third approach is further refined to account for build orientation in addition to HT post-processing, referred to as the Post-Processing and Build Orientation Model (PBOM). Like the previous model, it uses categorical variables for the AB and HT conditions but also incorporates the build angle (BA) into the equation, providing a more comprehensive prediction of fatigue life based on both post-processing and orientation factors:

$$\text{For AB: } \log_{10}(\sigma_a) = 2.77 - (0.00383 + 0.0000118 \bullet \text{BA}) \bullet [\log_{10}(N)]^{2.69} \quad (14)$$

$$\text{For HT: } \log_{10}(\sigma_a) = (2.8 - 0.000521 \bullet \text{BA}) - (0.0191 - 0.0000233 \bullet \text{BA}) \bullet [\log_{10}(N)]^{1.83}$$

Metrics	Predictive approaches			
	RA	PLM	PM	PBOM
Percentage of data points outside the ± 2-factor error range	17.4%	39.1%	37.7%	29.0%
Percentage of data points outside the ± 3-factor error range	2.9%	18.8%	15.9%	11.6%
RMSE for log(N)	0.213 or ± 1.63-factor error	0.372 or ± 2.36-factor error	0.339 or ± 2.18-factor error	0.310 or ± 2.04-factor error
RMSE for σ_a	16.7 MPa	27.8 MPa	27.0 MPa	24.4 MPa

Table 4. Comparison of the predictive approaches.

Notably, material parameters that showed minimal variation across BA (e.g., the term 2.77 in Eq. 14) were treated as constants. These adjustments had little impact on the overall accuracy of the model. To calculate the model parameters, the least squares method was applied.

Figure 8 illustrates the prediction results of the PBOM model, with fatigue life predictions presented for different BA at AB and HT conditions. As shown in Fig. 8a, the predicted fatigue life for HT parts shows little variation across different BA in the high-cycle region, with all the curves converging to a single one. This indicates that the influence of BA becomes negligible after HT at higher fatigue cycles. Conversely, the PBOM model highlights a significant influence of BA on fatigue life for AB parts in the high-cycle region (Fig. 8b). In particular, the model predicts that AB parts printed at 0 degrees exhibit superior fatigue performance, while those printed at 90 degrees are expected to have notably worse fatigue properties. This suggests that BA plays a more critical role in fatigue performance when no HT, like ANN, is applied, and this effect diminishes once HT is introduced.

Figure 8c shows that 49 out of 69 samples fall within the ± 2-factor error range, meaning 29.0% of the results are beyond this threshold. Additionally, 8 out of 69 samples (11.6%) fall outside the ± 3-factor error range. The RMSE between predicted and experimental fatigue life values is approximately 0.310 on a logarithmic scale, corresponding to a ± 2.04-factor error, while the RMSE between predicted and experimental stress amplitude values is around 24.4 MPa. These results demonstrate a significant improvement in accuracy compared to previously considered models. The reduction in both the error range and RMSE highlights the model's enhanced predictive capability. By capturing the additional parameters, this method provides a more robust and precise prediction of fatigue life, making it superior to earlier approaches.

The comparison of the predictive approaches is presented in Table 4. According to the data, the RA demonstrates the highest accuracy, with its accuracy metrics being at least 1.5 times better than those of other models. However, despite its superior precision, the RA model has significant limitations in practical application. Firstly, it is essentially a collection of separate S-N curves (see Eqs. 1–10), each applied individually, making it difficult to transition from one curve to another during prediction interpretation. Another drawback is that the model is limited to the specific build orientations studied in this experimental work, making it unsuitable for intermediate angles, such as 50 degrees. Additionally, the RA approach requires a substantial amount of data to determine curve coefficients; for instance, the model used 14 curves for 7 build orientations in both AB and HT conditions, involving 42 different constants. Nevertheless, the RA can be considered a benchmark method for comparison purposes.

In contrast, the PBOM model offers greater flexibility and ease of interpretation, supporting predictions for intermediate angles and various post-processing conditions. It outperforms the PLM and PM models by approximately 22% and 19%, respectively, in terms of the percentage of points beyond a ± 2-factor error, and by 38% and 27% for points beyond a ± 3-factor error. Additionally, it shows improvements of 17% and 9% in RMSE for logarithmic fatigue life predictions, and 12% and 10% in RMSE for stress amplitude predictions. These results highlight the advantages of using the PBOM model over the simpler PLM and PM approaches.

The PBOM approach requires only 9 constants, which can be determined from 4 fatigue curves, for example, at 0 and 90 degrees of build orientation under both HT and AB conditions. However, PBOM assumes a linear relationship with BA, meaning it may require additional test data if non-linear effects are present. For instance, 2 more curves at 45 degrees under HT and AB conditions would be necessary to capture non-linear behavior. Fortunately, experimental data at 0, 45, and 90 degrees are frequently available in the literature, making it feasible to enhance the model using methods like polynomial regression to capture statistically significant effects. However, in this study, such complexity was not required, as the linear PBOM model adequately described the experimental data. This conclusion is supported by the fact that a scatter factor of less than three is generally regarded as acceptable[90,91], with nearly 90% of the data points for the PBOM model falling within this range.

Conclusions

The impact of small build orientation variations and heat treatment on the fatigue performance of selective laser melted 316 L stainless steel was investigated through quasi-static and cyclic tensile experiments, followed by predictive modeling.

The results show that ultimate tensile strength in the as-built condition varies modestly by 7%, while the heat-treated condition exhibits a greater variation of 13%. The influence of build angle on ultimate tensile strength is more pronounced in the heat-treated condition. However, the overall differences between as-built and heat-treated conditions remain relatively small.

Fatigue results reveal minimal variation between as-built and heat-treated states in the low-cycle region, but differences become more evident in the high-cycle region, with heat-treated samples generally outperforming

as-built ones. Build orientation has a stronger effect on fatigue performance in the as-built condition, especially in the high-cycle range. In as-built samples, fatigue life decreases as the build angle increases, with horizontally oriented samples performing better than vertically oriented ones.

For predictive modeling, a stepwise approach was adopted, progressively increasing model complexity across three stages: (1) applying a single power law function, (2) incorporating heat treatment post-processing, and (3) accounting for build orientation. The most advanced model, which includes post-processing and build orientation, outperforms simpler models across key metrics, showing 22% and 19% fewer points beyond the ± 2-factor error, 38% and 27% fewer points beyond the ± 3-factor error, and RMSE improvements of 17% and 9% for logarithmic fatigue life, along with 12% and 10% improvements for stress amplitude.

This model is efficient in terms of data requirements, needing only two fatigue curves for two build orientations per post-processing condition. Given that such data are often available in the literature, the model is broadly applicable for predicting fatigue behavior at various build angles. This makes it particularly useful for modeling complex structures, such as lattices, where struts can adopt a wide range of angles.

Data availability

All data generated or analysed during this study are included in this published article.

Received: 11 November 2024; Accepted: 3 February 2025
Published online: 07 February 2025

References

1. Srivastava, M., Rathee, S., Maheshwari, S. & Kundra, T. K. Additive manufacturing. CRC Press eBooks (2019). https://doi.org/10.1201/9781351049382
2. ASTM ISO/ASTM. 52900–21 Additive manufacturing — General principles — Fundamentals and vocabulary.
3. Phutela, C., Aboulkhair, N. T., Tuck, C. J. & Ashcroft, I. The effects of feature sizes in selectively laser melted Ti-6Al-4V parts on the validity of optimised process parameters. *Materials* **13**, 117 (2019).
4. Gillham, B. et al. Tailoring the theory of critical distances to better assess the combined effect of complex geometries and process-inherent defects during the fatigue assessment of SLM Ti-6Al-4V. *Int. J. Fatigue*. **172**, 107602 (2023).
5. Huang, Y. et al. Microstructure and wear properties of selective laser melting 316L. *Mater. Chem. Phys*. **254**, 123487 (2020).
6. Li, Y., Ge, Y., Lei, J. & Bai, W. Mechanical properties and constitutive model of selective laser melting 316L Stainless Steel at different scanning speeds. *Adv. Mater. Sci. Eng.* **2022**, 1–13 (2022).
7. Leary, M., Maconachie, T., Sarker, A., Faruque, O. & Brandt, M. Mechanical and thermal characterisation of AlSi10Mg SLM block support structures. *Mater. Design*. **183**, 108138 (2019).
8. Wu, H. et al. Selective laser melted AlSi10Mg alloy under melting mode transition: microstructure evolution, nanomechanical behaviors and tensile properties. *J. Alloys Compd.* **873**, 159823 (2021).
9. Balbaa, M., Mekhiel, S., Elbestawi, M. & McIsaac, J. On selective laser melting of Inconel 718: densification, surface roughness, and residual stresses. *Mater. Design*. **193**, 108818 (2020).
10. Avanzini, A. Fatigue Behavior of Additively Manufactured Stainless Steel 316L. *Materials* **16**, 65 (2022).
11. Sharma, S. K., Singh, A. K., Mishra, R. K., Shukla, A. K. & Sharma, C. Processing techniques, Microstructural and Mechanical Properties of Additive Manufactured 316L Stainless Steel: review. *J. Institution Eng. (India) Ser. D*. https://doi.org/10.1007/s40033-023-00497-4 (2023).
12. Uhlmann, E., Fleck, C., Gerlitzky, G. & Faltin, F. Dynamical fatigue behavior of Additive Manufactured products for a Fundamental Life cycle Approach. *Procedia CIRP*. **61**, 588–593 (2017).
13. Elangeswaran, C. et al. Effect of post-treatments on the fatigue behaviour of 316L stainless steel manufactured by laser powder bed fusion. *Int. J. Fatigue*. **123**, 31–39 (2019).
14. Hatami, S., Ma, T., Vuoristo, T., Bertilsson, J. & Lyckfeldt, O. Fatigue Strength of 316 L Stainless Steel Manufactured by selective laser melting. *J. Mater. Eng. Perform.* **29**, 3183–3194. https://doi.org/10.1007/s11665-020-04859-x (2020).
15. Hatami, S., Ma, T., Vuoristo, T., Bertilsson, J. & Lyckfeldt, O. Fatigue Strength of 316 L Stainless Steel Manufactured by selective laser melting. *J. Mater. Eng. Perform.* **29**, 3183–3194 (2020).
16. Spierings, A. B., Starr, T. L. & Wegener, K. Fatigue performance of additive manufactured metallic parts. *Rapid Prototyp. J.* **19**, 88–94 (2013).
17. Lai, W. J., Ojha, A., Li, Z., Engler-Pinto, C. & Su, X. Effect of residual stress on fatigue strength of 316L stainless steel produced by laser powder bed fusion process. *Progress Additive Manuf.* **6**, 375–383 (2021).
18. Wood, P., Libura, T., Kowalewski, Z. L., Williams, G. & Serjouei, A. Influences of Horizontal and Vertical Build orientations and Post-fabrication processes on the Fatigue Behavior of Stainless Steel 316L produced by selective laser melting. *Materials* **12**, 4203 (2019).
19. Rautio, T. et al. The effect of severe shot peening on Fatigue Life of Laser Powder Bed Fusion Manufactured 316L Stainless Steel. *Materials* **15**, 3517 (2022).
20. Afkhami, S., Dabiri, M., Piili, H. & Björk, T. Effects of manufacturing parameters and mechanical post-processing on stainless steel 316L processed by laser powder bed fusion. *Mater. Sci. Eng., a*. **802**, 140660 (2020).
21. Zulić, S. et al. Fatigue life enhancement of additive manufactured 316l stainless steel by LSP using a DPSS laser system. *Surf. Eng.* **38**, 183–190 (2022).
22. Zhang, M. et al. High cycle fatigue and ratcheting interaction of laser powder bed fusion stainless steel 316L: fracture behaviour and stress-based modelling. *Int. J. Fatigue*. **121**, 252–264 (2018).
23. Benarji, K., Kumar, Y. R., Jinoop, A. N., Paul, C. P. & Bindra, K. S. Effect of heat-treatment on the microstructure, Mechanical properties and Corrosion Behaviour of SS 316 structures built by Laser Directed Energy Deposition based Additive Manufacturing. *Met. Mater. Int.* **27**, 488–499 (2020).
24. Leuders, S., Lieneke, T., Lammers, S., Tröster, T. & Niendorf, T. On the fatigue properties of metals manufactured by selective laser melting – the role of ductility. *J. Mater. Research/Pratt's Guide Venture Capital Sources*. **29**, 1911–1919 (2014).
25. Zeng, F., Yang, Y. & Qian, G. Fatigue properties and S-N curve estimating of 316L stainless steel prepared by SLM. *Int. J. Fatigue*. **162**, 106946 (2022).
26. Mower, T. M. & Long, M. J. Mechanical behavior of additive manufactured, powder-bed laser-fused materials. *Mater. Sci. Eng., a*. **651**, 198–213 (2015).
27. Elangeswaran, C., Cutolo, A., Muralidharan, G. K., Vanmeensel, K. & Van Hooreweder, B. Microstructural analysis and fatigue crack initiation modelling of additively manufactured 316L after different heat treatments. *Mater. Design*. **194**, 108962 (2020).
28. Aiza, I. et al. Effects of build orientation and inclined features on physical, microstructural and mechanical properties of powder bed fusion additively manufactured metallic parts. *Prog. Mater. Sci.* **147**, 101357 (2024).

29. Shrestha, R., Simsiriwong, J., Shamsaei, N., Thompson, S. M. & Bian, L. Effect of Build Orientation on the Fatigue Behavior of Stainless Steel 316L Manufactured via a Laser-Powder Bed Fusion Process. at (2016). https://hdl.handle.net/2152/89615
30. Ponticelli, G. S., Panciroli, R., Venettacci, S., Tagliaferri, F. & Guarino, S. Experimental investigation on the fatigue behavior of laser powder bed fused 316L stainless steel. *CIRP J. Manufact. Sci. Technol.* **38**, 787–800 (2022).
31. Beard, W., Lancaster, R., Barnard, N., Jones, T. & Adams, J. The influence of surface finish and build orientation on the low cycle fatigue behaviour of laser powder bed fused stainless steel 316L. *Mater. Sci. Eng., a*. **864**, 144593 (2023).
32. Liang, X., Hor, A., Robert, C., Lin, F. & Morel, F. Effects of building direction and loading mode on the high cycle fatigue strength of the laser powder bed fusion 316L. *Int. J. Fatigue*. **170**, 107506 (2023).
33. Shrestha, R., Simsiriwong, J. & Shamsaei, N. Fatigue behavior of additive manufactured 316L stainless steel parts: effects of layer orientation and surface roughness. *Additive Manuf.* **28**, 23–38 (2019).
34. Murchio, S. et al. Additively manufactured Ti–6Al–4V thin struts via laser powder bed fusion: Effect of building orientation on geometrical accuracy and mechanical properties. *J. Mech. Behav. Biomedical Materials/Journal Mech. Behav. Biomedical Mater.* **119**, 104495 (2021).
35. Yankin, A., Seisekulova, A., Perveen, A. & Talamona, D. Mechanical properties of additively manufactured AlSi10Mg under quasi-static and cyclic loading. *Fatigue Fract. Eng. Mater. Struct.* **47**, 1696–1714 (2024).
36. Solberg, K., Hovig, E. W., Sørby, K. & Berto, F. Directional fatigue behaviour of maraging steel grade 300 produced by laser powder bed fusion. *Int. J. Fatigue*. **149**, 106229 (2021).
37. Qin, F. et al. Influence of powder particle size distribution on microstructure and mechanical properties of 17 – 4 PH stainless steel fabricated by selective laser melting. *J. Mater. Res. Technol.* **25**, 231–240 (2023).
38. Yankin, A. et al. Comprehensive analysis of ultrasonically atomized 316L stainless steel powder using adjusted additive manufacturing suitability factor. *Powder Technol.* **444**, 120004 (2024).
39. Waqar, S., Guo, K. & Sun, J. Evolution of residual stress behavior in selective laser melting (SLM) of 316L stainless steel through preheating and in-situ re-scanning techniques. *Opt. Laser Technol.* **149**, 107806 (2021).
40. Mertens, R. et al. Influence of Powder Bed Preheating on Microstructure and Mechanical Properties of H13 Tool Steel SLM parts. *Phys. Procedia*. **83**, 882–890 (2016).
41. Yang, M. et al. High-cycle fatigue behavior and fatigue strength prediction of differently heat-treated 35CrMo steels. *Metals* **12**, 688 (2022).
42. Usabiaga, H., Muniz-Calvente, M., Ramalle, M., Urresti, I. & Canteli, A. F. Improving with probabilistic and scale features the Basquin linear and bi-linear fatigue models. *Eng. Fail. Anal.* **116**, 104728 (2020).
43. Yankin, A., Wildemann, V., Belonogov, N. & Staroverov, O. Influence of static mean stresses on the fatigue behavior of 2024 aluminum alloy under multiaxial loading. *Frattura Ed. Integrità Strutturale*. **14**, 151–163 (2019).
44. Burhan, I. & Kim, H. S. N. Curve models for Composite materials Characterisation: an evaluative review. *J. Compos. Sci.* **2**, 38 (2018).
45. Barbosa, J. et al. A comparison between S-N logistic and Kohout-Věchet formulations applied to the fatigue data of old metallic bridges materials. *Frattura Ed. Integrità Strutturale*. **13**, 400–410 (2019).
46. Bathias There is no infinite fatigue life in metallic materials. *Fatigue Fract. Eng. Mater. Struct.* **22**, 559–565 (1999).
47. Kahraman, F. & Sagbas, A. An investigation of the effect of heat treatment on surface roughness in machining by using statistical analysis. *Iran. J. Sci. Technol. Trans. B: Eng.* **34**, 5, 591–595 (2010).
48. Taylor, D. *The Theory of Critical Distances: A New Perspective in Fracture Mechanics* (Elsevier, 2007).
49. Taylor, D. Applications of the theory of critical distances in failure analysis. *Eng. Fail. Anal.* **18**, 543–549 (2011).
50. Susmel, L. & Taylor, D. A novel formulation of the theory of critical distances to estimate lifetime of notched components in the medium-cycle fatigue regime. *Fatigue Fract. Eng. Mater. Struct.* **30**, 567–581 (2007).
51. Lobanov, D. et al. The analysis of stress raisers affecting the GFRP strength at quasi-static and cyclic loads by the theory of critical distances, digital image correlation, and Acoustic Emission. *Polymers* **15**, 2087 (2023).
52. Taylor, D. Microstructural parameters in the theory of critical distances. *Mater. Sci. Forum*. **567–568**, 23–28 (2007).
53. Cirik, E. & Genel, K. Effect of anodic oxidation on fatigue performance of 7075-T6 alloy. *Surf. Coat. Technol.* **202**, 5190–5201 (2008).
54. Xi, F. et al. Effects of substrate roughness on microstructure and fatigue behavior of plasma Electrolytic Oxidation-Coated Ti-6Al-4V Alloy. *Materials* **15**, 4256 (2022).
55. Lima, G. D. et al. Fatigue behavior and life predictions of thermally oxidized Ti6Al4V alloy according to oxidation parameters. *Eng. Fail. Anal.* **130**, 105737 (2021).
56. Li, Z. et al. Effect of Heat Treatment on Fatigue Performance of 316L Stainless Steel Fabricated by Laser Powder Bed Fusion. *J. Eng. Mater. Technol.* **146**, 1–35 (2024).
57. Röttger, A. et al. Microstructure and mechanical properties of 316L austenitic stainless steel processed by different SLM devices. *Int. J. Adv. Manuf. Technol.* **108**, 769–783 (2020).
58. Zhai, W., Zhou, W. & Nai, S. M. L. Grain refinement and strengthening of 316L stainless steel through addition of TiC nanoparticles and selective laser melting. *Mater. Sci. Engineering: A*. **832**, 142460 (2022).
59. Yang, D. et al. The mechanism of substructure formation and grain growth 316L stainless steel by selective laser melting. *Mater. Res. Express*. **8**, 096510 (2021).
60. Li, X. et al. Study on Mechanism of Structure Angle on Microstructure and Properties of SLM-Fabricated 316L Stainless Steel. *Front. Bioeng. Biotechnol.* **9**, 778332 (2021).
61. Zhao, C. et al. Influence of scanning strategy and building direction on microstructure and corrosion behaviour of selective laser melted 316L stainless steel. *Mater. Design*. **209**, 109999 (2021).
62. Petroušek, P. et al. Investigation of the Properties of 316L Stainless Steel after AM and Heat Treatment. *Materials* **16**, 3935 (2023).
63. Feng, Z., Pan, H., Wu, W., Wang, Z. & Jiang, P. Impact of Heat Treatment and Building Direction on Selective Laser-Melted 316L Stainless Steel: Microstructure and Mechanical Properties. Materials vol. 18 32 (2024).
64. Yan, X., Pang, J. & Jing, Y. Ultrasonic Measurement of Stress in SLM 316L Stainless Steel Forming Parts Manufactured using different scanning strategies. *Materials* **12**, 2719 (2019).
65. Prashanth, K. G. & Eckert, J. Formation of metastable cellular microstructures in selective laser melted alloys. *J. Alloys Compd.* **707**, 27–34 (2017).
66. Saeidi, K., Gao, X., Zhong, Y. & Shen, Z. J. Hardened austenite steel with columnar sub-grain structure formed by laser melting. *Mater. Sci. Engineering: A*. **625**, 221–229 (2015).
67. Zhu, W. et al. A multi-scale experimental investigation for fatigue limit and fatigue crack initiation behavior of powder bed fusion-laser beam 316L stainless steel. *Mater. Sci. Engineering: A*. **866**, 144692 (2023).
68. Kamaya, M. Influence of grain size on fatigue strength of austenitic stainless steel (investigation of ultimate strength dependency of fatigue strength). *Int. J. Fatigue*. **177**, 107947 (2023).
69. Xu, Z., Liu, A. & Wang, X. Fatigue performance and crack propagation behavior of selective laser melted AlSi10Mg in 0°, 15°, 45° and 90° building directions. *Mater. Sci. Engineering: A*. **812**, 141141 (2021).
70. Ning, J., Sievers, D. E., Garmestani, H. & Liang, S. Y. Analytical modeling of In-Process temperature in Powder Bed Additive Manufacturing considering laser power absorption, latent heat, scanning strategy, and powder packing. *Materials* **12**, 808 (2019).
71. Aversa, A. et al. Effect of process and Post-process conditions on the Mechanical properties of an A357 Alloy Produced via Laser Powder Bed Fusion. *Metals* **7**, 68 (2017).

72. Boes, J., Röttger, A., Mutke, C., Escher, C. & Theisen, W. Microstructure and mechanical properties of X65MoCrWV3-2 cold-work tool steel produced by selective laser melting. *Additive Manuf.* **23**, 170–180 (2018).
73. Beretta, S., Gargourimotlagh, M., Foletti, S., du Plessis, A. & Riccio, M. Fatigue strength assessment of as built AlSi10Mg manufactured by SLM with different build orientations. *Int. J. Fatigue*. **139**, 105737 (2020).
74. Tascioglu, E., Karabulut, Y. & Kaynak, Y. Influence of heat treatment temperature on the microstructural, mechanical, and wear behavior of 316L stainless steel fabricated by laser powder bed additive manufacturing. *Int. J. Adv. Manuf. Technol.* **107**, 1947–1956 (2020).
75. Salarvand, V. et al. Microstructure and corrosion evaluation of as-built and heat-treated 316L stainless steel manufactured by laser powder bed fusion. *J. Mater. Res. Technol.* **18**, 4104–4113 (2022).
76. Salman, O. O., Gammer, C., Chaubey, A. K., Eckert, J. & Scudino, S. Effect of heat treatment on microstructure and mechanical properties of 316L steel synthesized by selective laser melting. *Mater. Sci. Engineering: A*. **748**, 205–212 (2019).
77. Kong, D. et al. Mechanical properties and corrosion behavior of selective laser melted 316L stainless steel after different heat treatment processes. *J. Mater. Sci. Technol.* **35**, 1499–1507 (2019).
78. Chao, Q. et al. The effect of post-processing heat treatment on the microstructure, residual stress and mechanical properties of selective laser melted 316L stainless steel. *Mater. Sci. Engineering: A*. **821**, 141611 (2021).
79. Morozova, I. et al. On the Heat treatment of selective-laser-melted 316L. *J. Mater. Eng. Perform.* **32**, 4295–4305 (2022).
80. Birnbaum, A. J., Steuben, J. C., Barrick, E. J., Iliopoulos, A. P. & Michopoulos, J. G. Intrinsic strain aging, Σ3 boundaries, and origins of cellular substructure in additively manufactured 316L. *Additive Manuf.* **29**, 100784 (2019).
81. Kong, D. et al. About metastable cellular structure in additively manufactured austenitic stainless steels. *Additive Manuf.* **38**, 101804 (2021).
82. Diepold, B. et al. Temperature-dependent dynamic strain aging in selective laser melted 316L. *Adv. Eng. Mater.* **23,** 2001501 (2021).
83. Everitt, B. S. & Skrondal, A. *The Cambridge Dictionary of Statistics. Fourthed* (Cambridge University Press, 2010).
84. Kaiser, R., Williamson, K., O'Brien, C., Ramirez-Garcia, S. & Browne, D. J. The influence of cooling conditions on grain size, secondary phase precipitates and mechanical properties of biomedical alloy specimens produced by investment casting. *J. Mech. Behav. Biomed. Mater.* **24**, 53–63 (2013).
85. Bian, Z. et al. An ML-Based Approach for HCF Life Prediction of Additively Manufactured AlSi10Mg considering the effects of Powder size and fatigue damage. *Aerospace* **10**, 586 (2023).
86. Zhao, E., Zhou, Q., Qu, W. & Wang, W. Fatigue Properties Estimation and Life Prediction for Steels under Axial, Torsional, and In-Phase Loading. Advances in Materials Science and Engineering (2020). (2020).
87. Yankin, A., Mugatarov, A. I. & Wildemann, V. E. Influence of different loading paths on the multiaxial fatigue behavior of 2024 aluminum alloy under the same amplitude values of the second invariant of the stress deviator tensor. *Frattura Ed. Integrità Strutturale*. **15**, 327–335 (2020).
88. Lobanov, D., Yankin, A. S. & Berdnikova, N. I. Statistical evaluation of the effect of hygrothermal aging on the interlaminar shear of GFRP. *Frattura Ed. Integrità Strutturale*. **16**, 146–157 (2022).
89. Yankin, A. et al. Optimization of fatigue performance of FDM ABS and Nylon printed parts. *Micromachines* **14**, 304 (2023).
90. Karolczuk, A., Skibicki, D. & Pejkowski, Ł. Gaussian process for machine learning-based fatigue life prediction model under Multiaxial stress–strain conditions. *Materials* **15**, 7797 (2022).
91. Wang, Y., Faruq, N. Z. & Susmel, L. Evaluation of different techniques in estimating orientation of crack initiation planes and fatigue lifetime under complex multiaxial loading paths. *Int. J. Fatigue*. **100**, 521–529 (2017).

Author contributions

CRediT authorship contribution statement: A.Y.: Writing - original draft, Investigation, Visualization, Data analysis. A.P.: Methodology, Writing - review & editing, Conceptualization. D.T.: Conceptualization, Supervision, Project administration, Funding acquisition, Resources.

Funding

This research was funded under the project "Design, fabrication & characterization of metal lattice structures using ultrasonically atomized powder" (grant no: 211123CRP1615) by Nazarbayev University.

Declarations

Competing interests

The authors declare no competing interests.

Additional information

Correspondence and requests for materials should be addressed to D.T.

Reprints and permissions information is available at www.nature.com/reprints.

Publisher's note Springer Nature remains neutral with regard to jurisdictional claims in published maps and institutional affiliations.